The Astrophysical Journal, 979:14 (15pp), 2025 January 20 https://doi.org/10.3847/1538-4357/ad96bb


# An Indication of Gas Inflow in Clumpy Star-forming Galaxies near $z \sim 1$: Lower Gas-phase Metallicities in Clumpy Galaxies Compared to Nonclumpy Galaxies

Visal Sok[1], Adam Muzzin[1], Pascale Jablonka[2], Vivian Yun Yan Tan[1], Z. Cemile Marsan[1], Danilo Marchesini[3], Gillian Wilson[4], and Leo Y. Alcorn[5]
[1] Department of Physics and Astronomy, York University, 4700 Keele Street, Toronto, ON M3J 1P3, Canada; sokvisal@yorku.ca
[2] Laboratoire d'astrophysique, École Polytechnique Fédérale de Lausanne (EPFL), CH-1290 Sauverny, Switzerland
[3] Department of Physics & Astronomy, Tufts University, 419 Boston Avenue, Medford, MA 02155, USA
[4] Department of Physics, University of California Merced, 5200 Lake Road, Merced, CA 95343, USA
[5] David A. Dunlap Department of Astronomy & Astrophysics, University of Toronto, 50 Saint George Street, Toronto, ON M5S 3H4, Canada
*Received 2024 January 25; revised 2024 October 28; accepted 2024 November 19; published 2025 January 14*

## Abstract

Despite the ubiquity of clumpy star-forming galaxies at high-redshift, the origin of clumps are still largely unconstrained due to the limited observations that can validate the mechanisms for clump formation. We postulate that if clumps form due to the accretion of metal-poor gas that leads to violent disk instability, clumpy galaxies should have lower gas-phase metallicities compared to nonclumpy galaxies. In this work, we obtain the near-infrared spectrum for 42 clumpy and nonclumpy star-forming galaxies of similar masses, star formation rates, and colors at $z \approx 0.7$ using the Gemini Near-Infrared Spectrograph (GNIRS) and infer their gas-phase metallicity from the [N II]$\lambda$6584 and H$\alpha$ line ratio. We find that clumpy galaxies have lower metallicities compared to nonclumpy galaxies, with an offset in the weighted average metallicity of $0.07 \pm 0.02$ dex. We also find an offset of $0.06 \pm 0.02$ dex between clumpy and nonclumpy galaxies in a comparable sample of 23 star-forming galaxies at $z \approx 1.5$ using existing data from the FMOS-COSMOS survey. Similarly, lower [N II]$\lambda$6584/H$\alpha$ ratios are typically found in galaxies that have more of their $UV_{rest}$ luminosity originating from clumps, suggesting that clumpier galaxies are more metal-poor. We also derive the intrinsic velocity dispersion and line-of-sight rotational velocity for galaxies from the GNIRS sample. The majority of galaxies have $\sigma_0/v_c \approx 0.2$, with no significant difference between clumpy and nonclumpy galaxies. Our result indicates that clump formation may be related to the inflow of metal-poor gas; however, the process that forms them does not necessarily require significant, long-term kinematic instability in the disk.

*Unified Astronomy Thesaurus concepts:* Galaxy evolution (594); Galaxy formation (595); Galaxy kinematics (602); Metallicity (1031); Star forming regions (1565)

## 1. Introduction

An important step to understanding the formation and evolution of galaxies is to trace where star formation is occurring within galaxies through cosmic time. Deep field observations reveal an abundance of high-redshift star-forming galaxies (SFGs) that host prominent, clumpy star formation (S. Wuyts et al. 2012; K. L. Murata et al. 2014; Y. Guo et al. 2015; N. M. Förster Schreiber et al. 2018; V. Sok et al. 2022; Z. Sattari et al. 2023). Interestingly, the fraction of clumpy galaxies evolves with the cosmic star formation rate density, where it peaks at cosmic noon before declining toward higher redshift (T. Shibuya et al. 2016); however, recent results from gravitationally lensed galaxies observed with JWST suggest clumpy star formation may dominate the mass assembly of galaxies at $z > 4$ (e.g., E. Vanzella et al. 2022; A. Adamo et al. 2024; L. Mowla et al. 2024). Star-forming clumps are observed as UV-bright, kiloparsec-scale structures, but are also detected in H$\alpha$ emission. The specific star formation rate (sSFR) of clumps is elevated compared to the surrounding regions (S. Wuyts et al. 2012, 2013). A gradient in the sSFR of clumps is also reported by Y. Guo et al. (2018), where clumps that are further away from the galactic centers typically have higher sSFR. They found a similar negative gradient in stellar masses and ages, possibly suggesting an inward migration of clumps. In general, clumps have estimated stellar masses of $10^7$–$10^9 M_\odot$ (e.g., E. Soto et al. 2017; A. Zanella et al. 2019; M. Huertas-Company et al. 2020), with lower-mass estimates reported in lensed galaxies (A. Cava et al. 2018). Nonetheless, the ubiquity and unique mode of clumpy star formation during a period known for galaxy mass assembly suggest that clumps play an integral role in galaxy formation.

The two commonly accepted modes for the formation of star-forming clumps are (1) in situ origins induced by violent disk instability (VDI), and (2) ex situ origins induced by merger events. In the former case, clumps form due to the fragmentation of unstable regions within a gas-rich disk (e.g., O. Agertz et al. 2009; A. Dekel et al. 2009b; D. Ceverino et al. 2010), with instabilities predicted by the Toomre $Q$ stability parameter (A. Toomre 1964). Such gas-rich disks are suggested to be continuously fed by cosmological gas stream (A. Dekel et al. 2009a). Supporting observational evidence for clump formation via VDI comes from the analyses of the coevolution of the clumpy fraction, merger rates, and disk instability rates, which suggests that mergers alone cannot fully explain clump formation at $z \sim 2$ (e.g., Y. Guo et al. 2015; D. Adams et al. 2022; Z. Sattari et al. 2023). Furthermore, A. Martin et al. (2023) argue that the higher star formation found in clumpy

galaxies compared to nonclumpy galaxies is unlikely explained by mergers alone, and therefore must be due to some internal processes. Similarly, the observed stellar mass function of clumps is also consistent with clumps having an in situ origin (M. Dessauges-Zavadsky & A. Adamo 2018; M. Huertas-Company et al. 2020).

Although there is strong evidence for VDI-driven formation of clumps, clump formation via merger events is also supported by several studies. Y. Guo et al. (2015) argue that minor mergers may drive clump formation in low-mass galaxies, whereas VDI dominates in high-mass galaxies. Merger-driven clump formation may also be more important at higher redshifts (e.g., $z > 4$) because higher merger rates are observed at earlier times (K. Duncan et al. 2019; T. Shibuya et al. 2022; Q. Duan et al. 2024). These merger-induced clumps are more commonly observed in simulations of major mergers at $z > 6$ (Y. Nakazato et al. 2024).

Under the VDI framework, we postulate that if clumps form within a gas-rich disk that is replenished by (relatively) pristine gas from cosmological accretion, it is expected that the accreting gas would dilute the metal contents within the disk, leading to lower metallicities in clumpy galaxies compared to nonclumpy galaxies. Indeed, such a scenario has been observed in a simulation by D. Ceverino et al. (2016), where clumps are found to have lower metallicities by 0.3 dex compared to the surrounding regions. Therefore, one way for testing in situ clumpy formation is to compare the metallicity of the gas disk for clumpy and nonclumpy galaxies (i.e., galaxies that do not host star-forming clumps).

In this work, we use the Gemini-North Near-infrared Spectrograph (GNIRS) on the Gemini-North observatory to indirectly measure the gas-phase metallicity for a sample of clumpy and nonclumpy galaxies at $z \approx 0.7$ and test the validity of clump formation under VDI. We also make use of another large near-infrared spectroscopic survey (FMOS-COSMOS; J. D. Silverman et al. 2015; D. Kashino et al. 2019), which will serve as an independent test to see if the metallicity offset is observed in a different sample of SFGs at $z \approx 1.5$. The metallicity is inferred from the [N II]$\lambda$6584 and H$\alpha$ line ratio, following the calibration from M. Pettini & B. E. J. Pagel (2004). This line ratio is commonly used because both lines are easily accessible from the same filter, and their proximity mitigates the effect of dust in the inferred metallicity.

The structure of this paper is as follows. We discuss our galaxy sample, as well as define the nomenclature for clumpy and nonclumpy galaxies in Section 2. Overviews of the GNIRS observations and data reduction are then reported in Sections 3 and 4, respectively. In Section 5, we present our metallicity measurements and compare them to other studies. Given the high signal-to-noise ratio (SNR) of some of our spectra, we also investigate the relation between disk kinematics and morphologies (i.e., clumpy versus nonclumpy) in Section 6. Finally, we discuss the implications of our results in the context of clump formation due to VDI in Section 7.

Throughout this paper, we adopt a $\Lambda$CDM cosmological model of the universe with $\Omega_\lambda = 0.7$, $\Omega_M = 0.3$, and a Hubble constant of $H_0 = 70\,\mathrm{km\,s^{-1}\,Mpc^{-1}}$. All physical parameters are determined by assuming a Chabrier initial mass function (G. Chabrier 2003), and our magnitudes are reported in AB magnitudes.

## 2. Galaxy Sample

### 2.1. GNIRS Sample

Our targets are selected using the publicly available photometry of the COSMOS/UltraVISTA catalog (A. Muzzin et al. 2013). A number of criteria are employed to determine the candidates. We first require that the galaxies are at a redshift, either photometric or spectroscopic where available, where both H$\alpha$ and [N II]$\lambda$6584 lie within the wavelength coverage of the $X$ and $J$ filter of GNIRS, which avoid the highly contaminated atmospheric skylines in the $H$-band. The choice in the two GNIRS filters correspond to the detection of H$\alpha$ and [N II]$\lambda$6584 between the redshift range of $0.6 < z < 0.9$.

Using the stellar masses and SFRs from the UltraVISTA catalog, we then select galaxies of similar masses and SFRs to ensure that any observed metallicity offset is not driven by the fundamental metallicity relation (FMR). The masses were derived by fitting the spectral energy distribution (SED) of 30 photometric filters, extending from 0.15 to 24 $\mu$m, and the SFRs were determined from the rest-frame UV and infrared luminosity. We select primarily galaxies with $\log(M_*/M_\odot) \approx 10.5$. This corresponds to SFGs with a high SFR ($\gtrsim 10 M_\odot\,\mathrm{yr^{-1}}$), and therefore increases the likelihood of a strong detection for both H$\alpha$ and [N II]$\lambda$6584. Finally, we select galaxies of similar colors (i.e., $U - V$ and $V - J$) to mitigate the effect of dust in our analyses because galaxies with higher dust attenuation generally have higher metallicities.

Figure 1 summarizes our GNIRS galaxy sample. We select 42 galaxies, 23 are clumpy galaxies and 19 are nonclumpy galaxies (the classification of clumpy and nonclumpy is presented in Section 2.4). The solid markers denote galaxies that have a detection of SNR $> 3$ in both H$\alpha$ and [N II]$\lambda$6584. Throughout the analysis, we use only these S/N $> 3$ galaxies, which reduces our sample to 32 galaxies. The average mass for the clumpy galaxies is $\log(M_*/M_\odot) = 10.48^{+0.15}_{-0.02}$, with an average SFR of $\log(\mathrm{SFR}\,[M_\odot\,\mathrm{yr^{-1}}]) = 1.23^{+0.19}_{-0.14}$. The average mass for nonclumpy galaxies is $\log(M_*/M_\odot) = 10.54^{+0.04}_{-0.06}$, and their average SFR is $\log(\mathrm{SFR}\ \ [M_\odot\ \ \mathrm{yr^{-1}}]) = 1.30^{+0.12}_{-0.28}$. The average specific SFR for both clumpy and nonclumpy galaxies is approximately $\log(\mathrm{sSFR}\ \ [\mathrm{yr^{-1}}]) \approx -9.2$. Similarly, clumpy galaxies have an average $U - J = 1.21^{+0.11}_{-0.07}$ and $V - J = 0.95^{+0.11}_{-0.08}$, and for nonclumpy galaxies, $U - J = 1.32^{+0.08}_{-0.11}$ and $V - J = 1.05^{+0.06}_{-0.08}$. Here, the lower and upper errors are derived from the 16th and 84th percentiles.

### 2.2. FMOS-COSMOS Sample

The FMOS-COSMOS near-infrared spectroscopic survey (J. D. Silverman et al. 2015; D. Kashino et al. 2019) utilized the Fiber-Multi Object Spectrograph on the Subaru Telescope, and was comprised of an observing mode that primarily targets SFGs at $z \approx 1.5$. In particular, the survey provides fluxes for both H$\alpha$ and [N II]$\lambda$6584. The primary goal of this sample is to test whether a metallicity offset is also detected for a completely different sample of galaxies that have been observed with a different observing strategy, but are selected similarly in masses, SFRs, and colors as the GNIRS sample.

We crossmatch galaxies from the FMOS catalog to the UltraVISTA catalog, keeping only galaxies that have a measured R.A. and decl. that are within $0\farcs2$ of both catalogs. This angular scale corresponds to less than two imaging pixels

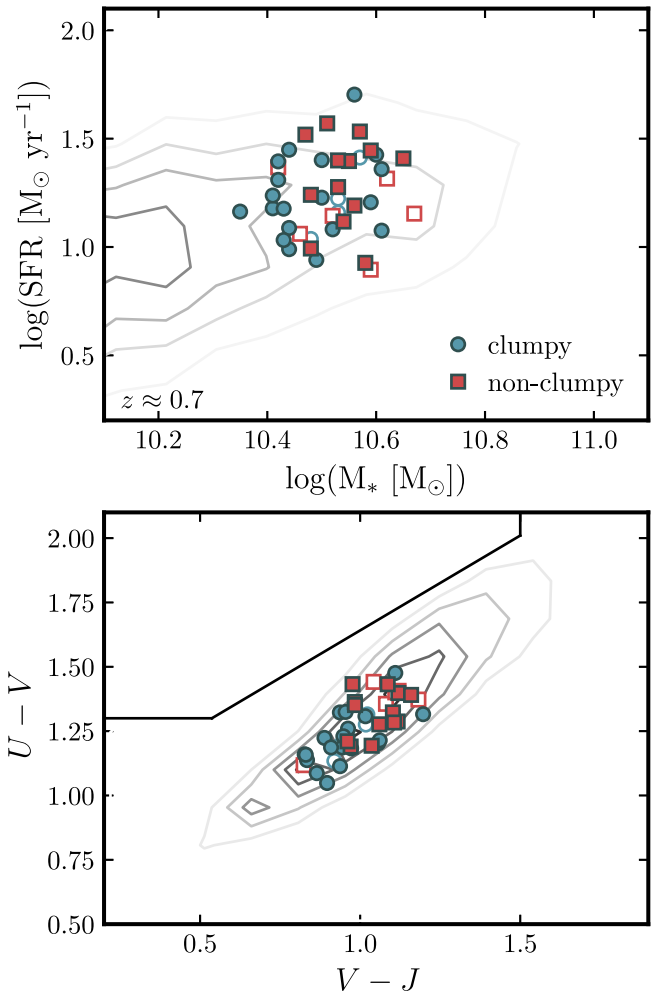


**Figure 1.** Top panel: The contour lines show the star-forming main sequence for the parent sample of galaxies at $z \approx 0.7$ in the COSMOS field. The blue circle and red square markers denote clumpy and nonclumpy galaxies that were observed with GNIRS, respectively. The solid markers denote galaxies with detection in both H$\alpha$ and [N II]$\lambda$6584 (SNR $> 3$). Bottom panel: Similar to the top panel, but now showing the *UVJ* diagram. In general, the selection process is limited to galaxies of similar masses, SFRs, and colors. This ensures that we can directly test for a relation between clumpy morphologies and metallicities.

of the UltraVISTA/COSMOS mosaics (which has a pixel scale of 0.″15). This is also well below the size of the images' point-spread function, and therefore ensures that there is no contamination from close-by neighbors. We select FMOS galaxies that have H$\alpha$ and [N II]$\lambda$6584 fluxes detected to at least 3$\sigma$. Similar to the GNIRS sample, we also select galaxies within a mass range between $10.4 < \log(M_*/M_\odot) < 10.6$, and limit the analyses to galaxies of similar colors, i.e., $0.9 < U - V < 1.2$ and $0.7 < V - J < 1.1$. In total, there are 23 FMOS galaxies at $z \approx 1.5$ that meet our selection criteria. We reiterate that the goal for this sample is mainly to determine whether a metallicity offset is similarly observed between clumpy and nonclumpy galaxies when using a different sample of galaxies. In the following sections, we discuss how galaxies are classified as clumpy and nonclumpy from their ground-based images.

### 2.3. Resolving Clumps with Finite-resolution Deconvolution

While clumpy galaxies are ubiquitous at high-redshift, identifying galaxies as clumpy is difficult due to the fact that high-resolution observations are required to resolve the kilo-parsec-scale structures. Furthermore, multiwavelength images are typically needed to account for the morphological *K*-correction effect, in which the morphology of galaxies may change depending on which wavelength they are observed in. This becomes particularly important when the galaxies are observed over a wide range of redshifts.

A unique solution to obtaining high-resolution and multi-wavelength imaging for a large volume of the sky is to use image deconvolution. This had been previously done in V. Sok et al. (2022) using finite-resolution deconvolution (FIREDEC; N. Cantale et al. 2016a), where we deconvolved the multiband imaging of approximately 20,000 SFGs in the COSMOS field at $0.5 < z < 2$, and created resolved stellar mass and surface brightness maps for those galaxies. That work showed that FIREDEC can recover clumps in galaxies from ground-based imaging. Comparing the deconvolved images to HST observations confirmed that these clumpy features are intrinsic to the galaxies and not artifacts of deconvolution.

A technical overview of image deconvolution and FIREDEC is provided in N. Cantale et al. (2016a), with practical applications discussed in N. Cantale et al. (2016b) and V. Sok et al. (2022). In summary, this deconvolution algorithm aims to deconvolve images to a finite resolution, ensuring that the resulting image retains its own point-spread function (PSF), i.e., as opposed to completely removing the PSF to achieve an infinite angular resolution, which would violate the Nyquist's sampling theorem. In practice, a target resolution is defined to be a two-dimensional Gaussian function. The deconvolution kernel is then constructed through a combination of analytical and numerical fits, such that the convolution between the deconvolution kernel and the Gaussian functions gives back the PSF of the image.

In order to deconvolve images in different filters of the COSMOS field, we constructed deconvolution kernels for each filter. This is required because the PSF can vary from filter to filter, which arises due to the different observing conditions (see V. Sok et al. 2022 for the PSF variation for each filter of the COSMOS field). Here, we deconvolved to an angular resolution of 0.″3, which probes a physical scale of approximately 2.3 kpc for galaxies at $z \approx 0.7$. While this angular resolution only partially resolves star-forming clumps, it is sufficient for identifying whether a galaxy is clumpy or nonclumpy. A comparison between the ground-based imaging and the deconvolved images for a few galaxies in this study is shown in Figure 2. These galaxies are chosen as examples because they have multiband HST imaging, which enables us to directly compare the deconvolved images to HST images. Galaxies that are classified as clumpy are denoted by the asterisk in the ID name in the right-hand panel. In general, deconvolution reveals multiple clumps that are not detectable with ground-based imaging. These clumps are also detected by HST, suggesting that the resolved clumps are intrinsic to the galaxies and are not deconvolution artifacts.

### 2.4. Clumpy/Nonclumpy Star-forming Galaxy Classification

A number of methods have been used to classify whether a galaxy is clumpy or nonclumpy. Clumps can be identified by creating a contrast image, in which an image is passed through a high-pass filter (e.g., A. Zanella et al. 2019; A. Claeyssens et al. 2023). The flux and size of the clumps can be obtained by fitting each clump with a Gaussian model. Recent studies have

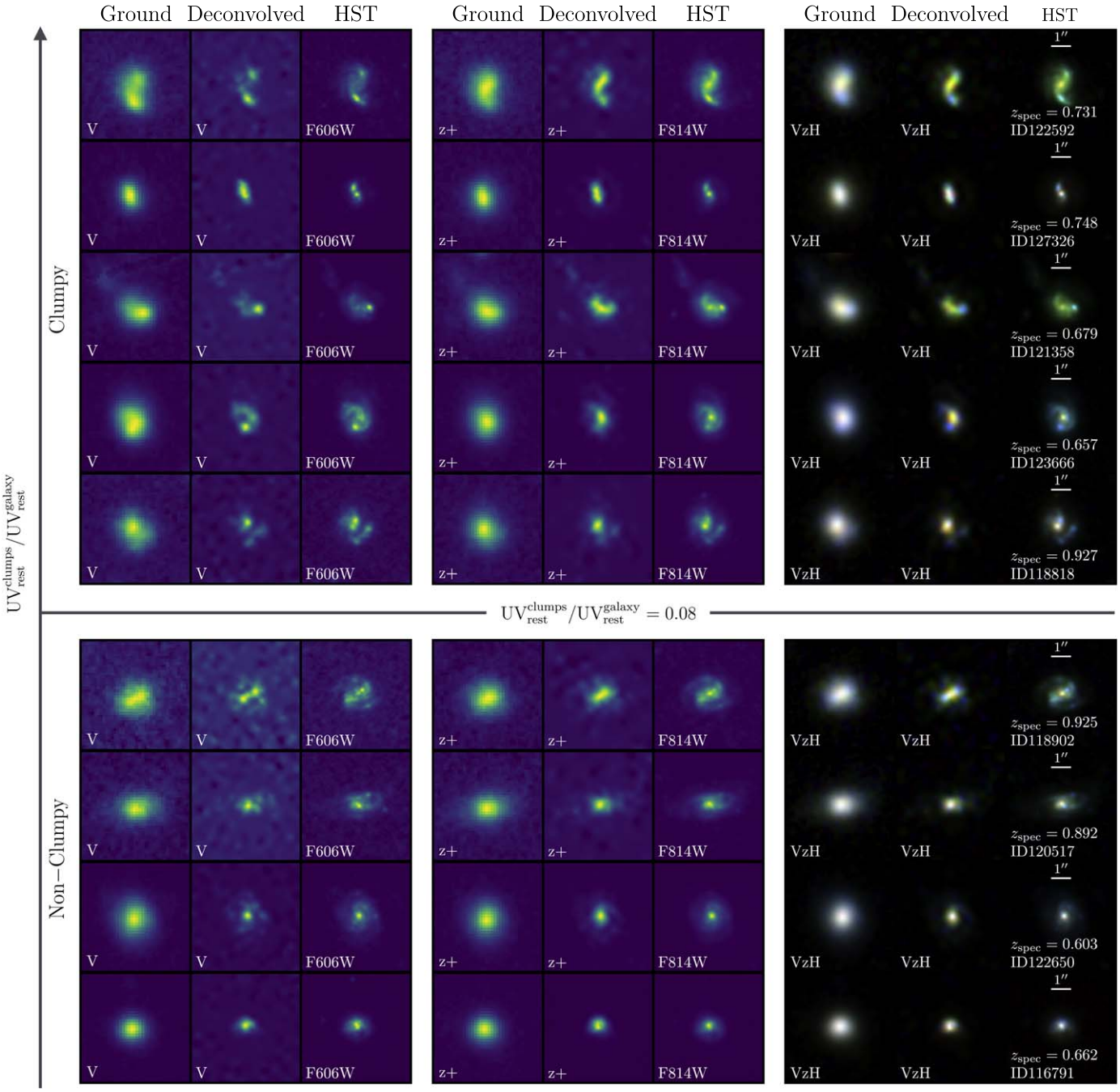


**Figure 2.** Comparison of deconvolved images to the corresponding HST images. From the left- to right-hand panels, we compare the *V*-band imaging to F606W, *z+*-band imaging to F814W, and the composite *VzH* image to a composite image constructed from F606W+F814W+F160W. Each stamp is $7\farcs8 \times 7\farcs8$. For each panel, the left- to right-hand column shows the ground-based image, the deconvolved image, and the corresponding HST image. Only nine out of the 42 galaxies from our sample have HST imaging in the three HST filters. The images are deconvolved to a resolution of $0\farcs3$, corresponding to a physical scale of ∼2.3 kpc at $z \approx 0.7$. We arrange the figure such that the galaxies are shown in ascending order based on their clumpiness, as defined by the ratio of rest-frame UV light emitted from clumps relative to the host galaxy. Clumpy galaxies are those with clumps that have at least 8% of the total rest-frame UV luminosity.

also employed a convolutional neural network to identify the location of clumps from an image (M. Huertas-Company et al. 2020).

In this work, we follow the method described in S. Wuyts et al. (2012), which utilizes the normalized rest-frame *U*-band light profile to identify clumpy regions in a galaxy. The rationale of a normalized profile relies on the fact that regions with relatively high surface brightness, such as UV-bright clumps, will appear as a bump in an otherwise smooth light profile of a galaxy. We will briefly describe the steps to making a normalized light profile; however, we refer the reader to S. Wuyts et al. (2012) for a more detailed process. We first obtain $U_{\mathrm{rest}}$ by spatially fitting the multiband deconvolved images with `EAZY` (G. B. Brammer 2008). Instead of fitting the SED over individual pixels, which can introduce biases for pixels with low SNR, we instead bin pixels using a Voronoi binning technique (`vorbin`; M. Cappellari & Y. Copin 2003) so that each Voronoi bin has a minimum SNR of 5 in the

*Ks*-band. A similar binning technique has been employed to construct stellar mass maps from spatially SED fits (S. Wuyts et al. 2012; V. Sok et al. 2022; V. Y. Y. Tan et al. 2022).

Once a map of the $U_{\rm rest}$ surface brightness is created, the normalized light profile for a galaxy is constructed. We characterize the galaxies by two elliptical parameters: the ellipticity and position angle. This is done by fitting an elliptical function to a segmentation map of the galaxy. These parameters are then used to define elliptical apertures centered on the galaxy. We then define the effective radius of the galaxy as the radius at which half of the light from the galaxy is within that radius. This is measured from a curve of growth based on the elliptical apertures. The effective surface brightness is then measured as the mean surface brightness within the effective radius. The normalized profile is constructed by normalizing the $U_{\rm rest}$ surface brightness at each pixel by the effective surface brightness, and the galactocentric distance of each pixel by the effective radius. In essence, the normalized profile illustrates how the normalized surface brightness varies with distance from the center of the galaxy. Figure 3 shows two examples of the normalized light profile for a clumpy and nonclumpy galaxy.

Clumps are situated in the same parameter space within the normalized profile. The division lines of the inner, outer, and clumpy regions, shown in Figure 3, are defined in Equations (6)–(8) of S. Wuyts et al. (2012), based on their visual inspections of the stacked profiles of their sample. Galaxies are defined as clumpy if they have pixels that originate from the clumpy regime in the normalized profile, and that contribute $\geqslant$8% of the total $U_{\rm rest}$ luminosity of the host galaxy. This criterion is commonly used to identify star-forming clumps in high-redshift galaxies in other studies, and therefore represents a consistent way of classifying clumpy galaxies.

## 3. GNIRS Observations

A total of 42 galaxies in the COSMOS field were observed with GNIRS by the Gemini-North observatory. These observations took place between 2019 and 2022 as part of several GNIRS observation programs, with program IDs: GN-2019B-Q-131, GN-2019B-Q-229, GN-2020A-Q-307, GN-2020B-Q-215, GN-2021B-Q-212, and GN-2022A-Q-213. The observations were done through the long-slit spectroscopy mode in the *X* or *J* filter and the 111 line per mm grating. We use the short camera, corresponding to a pixel resolution of 0.″15 per pixel, with a slit opening of 1″. The observational setup therefore corresponds to a wavelength coverage between 1.03 and 1.37 $\mu$m, at a spectral resolution of $R \approx 2000$ ($\sigma_{\rm inst} \sim 50\,{\rm km\,s^{-1}}$). This spectral resolution is sufficient for differentiating the H$\alpha$ and [N II]$\lambda$6584 emission lines. The on-source integration time for each galaxy is set to either 40 or 60 minutes. The shorter integration time is used when the observations took place with good seeing (i.e., Band 1) condition, while the longer 60 minutes of integration is needed when observing in the degraded seeing of Band 3 to account for greater light loss through the 1″ wide slit opening.

A blind offset from a reference bright star (or a reference object when there are no nearby star) is needed in order to center the slit onto our faint galaxies. The position of the slit is fixed along the major axis of the galaxy to ensure that most of the light coming from the galaxy is captured by the slit. We observe each galaxy using the ABB′A′ pattern, which corresponds to the dithering nod of −1″, 6″, −6″, 1″ along the slit direction. This pattern is used for sky subtraction, but helps mitigate pixel persistence when observing bright objects such as a standard star. At each nodding position, we have 300 s of integration. The standard star is observed either before or after the exposures on the galaxy using the same observational setup. The spectroscopic observations of a standard star are needed in order to apply flux calibration for telluric absorption features in the near-infrared.

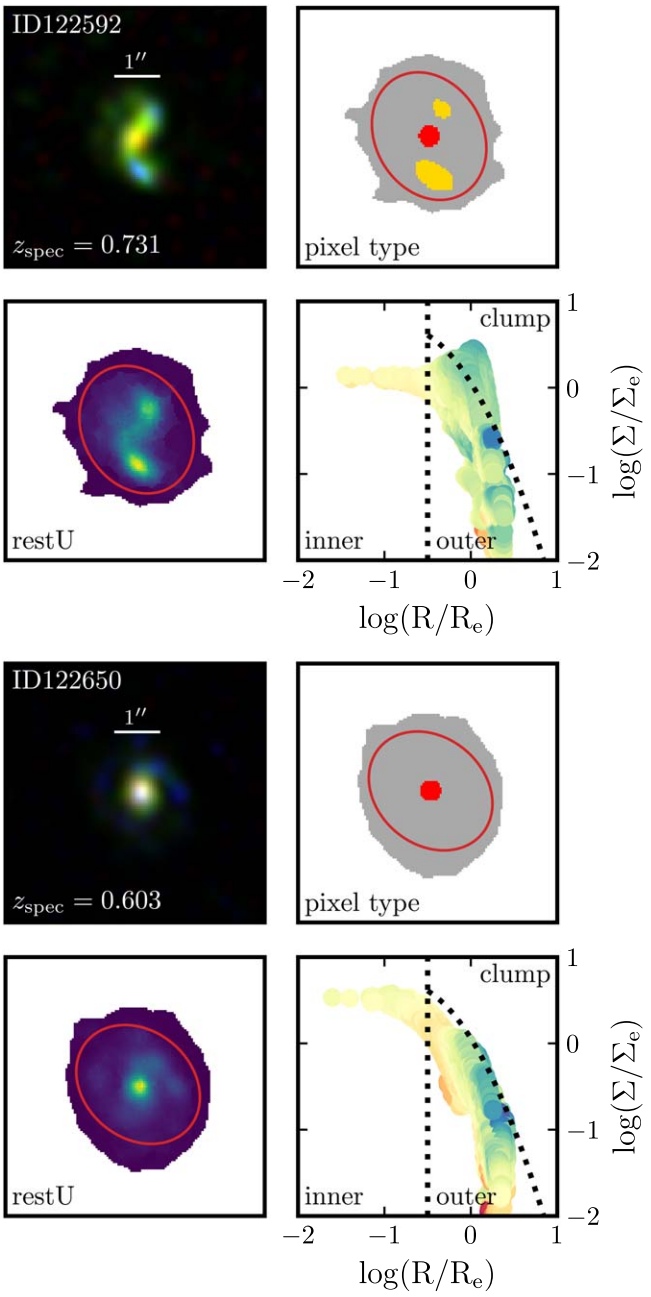


**Figure 3.** Two examples showing how the normalized light profile is used to identify clumps. The top figure shows the normalized profile for a clumpy galaxy while the bottom figure shows the profile for a nonclumpy galaxy. In each figure, the top left-hand panel shows the composite *VzH* image (6″ × 6″), the bottom left-hand panel shows the surface brightness, the bottom right-hand panel shows the constructed normalized $U_{\rm rest}$ profile, and top right-hand panel shows the pixel type map based on the division lines in the normalized light profile. The clump regime is defined as the pixel residing above the curved dotted line. As shown in the top figure in the pixel type map, clumps are identified easily using the normalized profile. The color-coding in the normalized profile respond to the $(U - V)_{\rm rest}$. Pixels in the clumpy regime are UV-bright.

## 4. Near-infrared Spectra

The reduction of the raw data is done using `Gemini IRAF` (Gemini Observatory & AURA 2016). A number of raw exposure frames for the science observations were affected by striping patterns; however, these patterns were removed with `cleanir`.[6] Telluric and science observations are then flat-fielded, sky-subtracted, and wavelength-calibrated. The master flat is obtained by stacking flat frames that do not have anomalous mean or standard deviation. The wavelength solution is computed by running `nswavelength` on the included Argon lamp observations. We extract the one-dimensional spectrum for the standard star using `nextract`. In the following sections, we describe the steps to extract the one-dimensional spectra from the reduced two-dimensional science spectra.

### 4.1. Spectra and Velocity Curves

One simple method for extracting a one-dimensional spectrum from the two-dimensional spectrum is the boxcar method, in which the two-dimensional spectrum is summed along the slit direction. However, this can lower the SNR of the emission lines if the galaxy's rotation is not accounted for. In this section, we describe the steps to extract the one-dimension spectrum by modeling the kinematics of the galaxy.

The kinematics modeling is performed using similar steps as outlined in B. J. Weiner et al. (2006). We first obtain the velocity and dispersion profile of a galaxy by fitting a Gaussian function to its emission lines along the slit. To this end, we bin the two-dimensional spectrum along the spatial direction by 2 pixels to increase the SNR of the emission lines. Here, H$\alpha$ is primarily used when fitting the Gaussian function because it has a higher SNR compared to [N II]$\lambda$6584. However, [N II]$\lambda$6584 is used when H$\alpha$ lies next to a strong skyline as the centroiding of the Gaussian function may be affected by the skyline. The fitted parameters are determined through a least-squares Levenberg–Marquardt minimization algorithm with respect to the observed data using `lmfit` (M. Newville et al. 2016). The retrieved error represents an uncertainty of one standard deviation around the fitted values. A few examples of the measured velocity profile are plotted in the right-hand panels of Figure 4.

The kinematics model consists of two components: a rotation curve and the dispersion term. We assume that the intrinsic velocity dispersion $\sigma_0$ is constant with radius for each galaxy. The inverse tangent function is adopted for the rotation of the galaxies,

$$v(r) = v_0 + \frac{2}{\pi} v_a \arctan\left(\frac{r - r_0}{r_t}\right), \quad (1)$$

where $v_a$ is asymptotic rotation velocity, $r_o$ is the spatial center of the galaxy, and $r_t$ is the knee radius to the flat part of the curve. When modeling the emission line, we vary values for $v_0$, $r_0$, $v_a$, and $\sigma_0$, while keeping $r_t$ constant at a fiducial value of $0\farcs2$ due to the limited seeing. The modeled emission line is then spatially convolved with a Gaussian seeing kernel. We determine the appropriate FWHM from the acquisition images of the bright offset star, or from the acquisition images of the standard star (which are observed before or after the science integration). The modeled emission line is also convolved by the line spread function. We use `emcee` (D. Foreman-Mackey et al. 2013) to explore the parameter space, assuming a flat prior for each parameter. The best-fit parameters and their errors are taken to be the median and standard deviation, respectively. We note that $\sigma_0$ is not resolved for a few galaxies due to our relatively coarse spectral resolution of $R \sim 2000$.

The rotation models are then used to align the emission lines along the slit. The one-dimensional, velocity-corrected spectrum are then optimally extracted, using the extraction algorithm from K. Horne (1986). The weighting profile is determined from the spatial profile of the emission lines. In cases where the emission lines have low SNR, we perform a standard boxcar extraction over some aperture width (i.e., $2\farcs1$ to $2\farcs7$ depending on the size of the galaxy). Finally, we do not apply an aperture correction for possible slit losses. While the size of galaxies varies and can therefore affect the measured [N II]$\lambda$6584/H$\alpha$ ratio, we mitigate this by placing the slit along the major axis that contains clumps. A slit correction would also assume some generalization of the metallicity gradient, which can be diverse (e.g., S. Gillman et al. 2021). However, larger galaxies typically have a negative metallicity gradient (D. Carton et al. 2018). Since clumpy galaxies are generally larger compared to nonclumpy galaxies (e.g., A. Martin et al. 2023), and assuming a negative metallicity gradient for clumpy galaxies, we expect the measured metallicity for clumpy galaxies to be overestimated compared to nonclumpy galaxies when using a slit that is centered on the central region of the galaxies. Given these reasons, we choose to not apply an uncertain slit-loss correction and present the data as is. Finally, we note that the size difference between nonclumpy and clumpy galaxies is observed for the GNIRS sample, where we find the average effective radius of clumpy and nonclumpy galaxies to be 5.1 $\pm$ 0.3 and 3.4 $\pm$ 0.3 kpc (corresponding to $0\farcs7$ and $0\farcs57$), respectively. Figure 4 summarizes this section, showing examples of the observed rotation in the two-dimensional spectrum, the derived velocity curve, and the extracted spectrum after correcting for the velocity curve.

### 4.2. Telluric Corrections

Molecules in the atmosphere can absorb and subsequently suppress certain spectral features in the near- and mid-infrared. These telluric absorption features may therefore affect the ratio between [N II]$\lambda$6584 and H$\alpha$ if the two lines fall within regions of strong absorption. Correcting for the absorption features is done by observing the spectrum of a standard star. Each of our observing blocks included a near-infrared spectroscopic observation of a standard star. The standard stars are selected to be early-type stars at a similar airmass, and are selected primarily because their spectra are generally devoid of intrinsic stellar absorption features in the near-infrared (between 1.05 and 1.3 $\mu$m), with the exception of hydrogen recombination lines. However, these hydrogen lines can be fitted and removed. The steps to apply the telluric correction to our observations are listed below.

1. Hydrogen absorption lines in the standard star telluric observations are first masked out. The continuum of the masked spectrum is modeled as the sum of Chebyshev polynomials using `specutils`.
2. The reference spectrum for each standard star is obtained from the stellar spectral library of A. J. Pickles (1998).

[6] https://github.com/andrewwstephens/cleanir

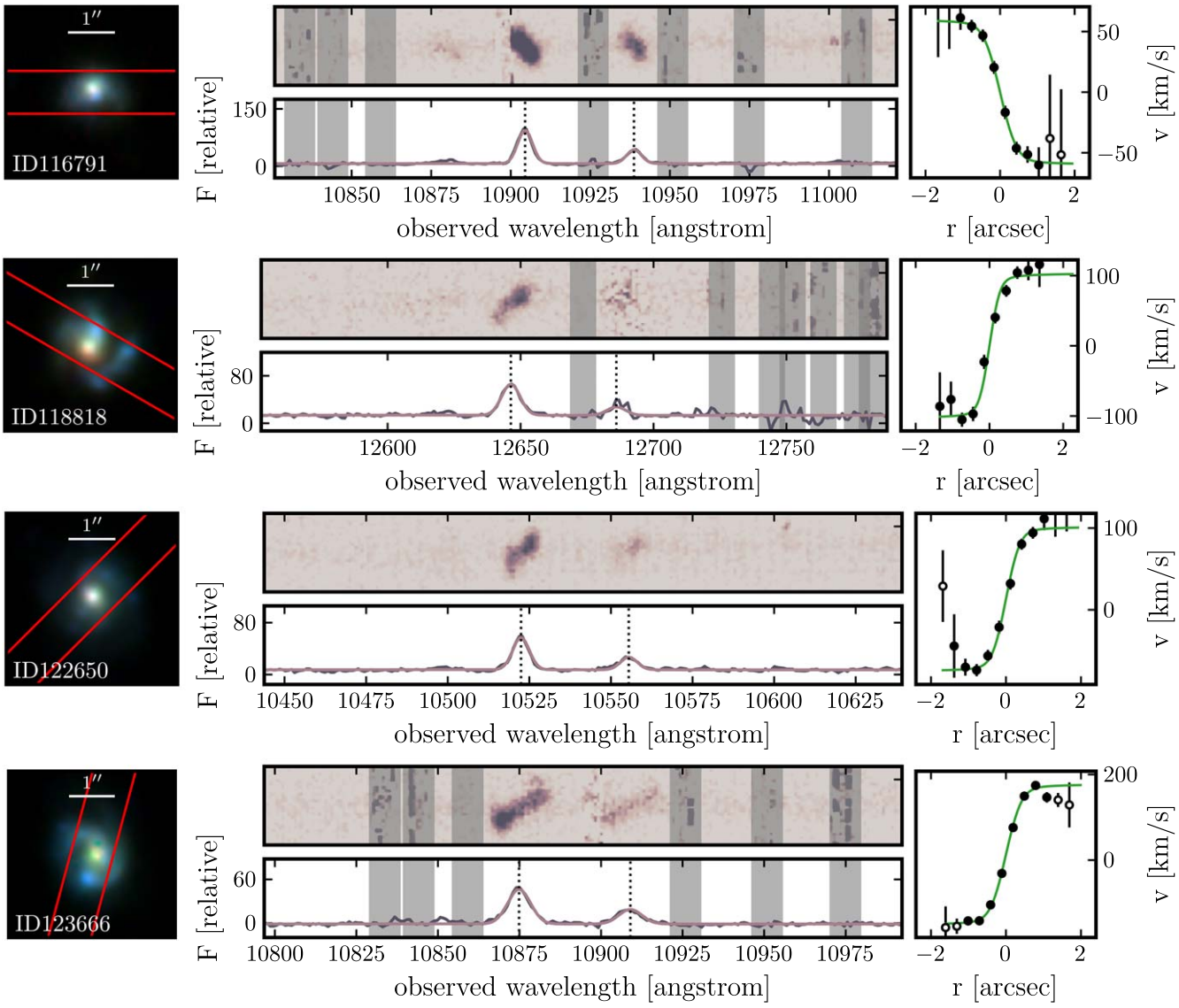


**Figure 4.** Examples of spectra along with the rotation curve of the galaxies. The left-hand panels show the composite image of the galaxies. The red line denotes the slit, which is purposely chosen to lie along the axis containing clumps. The top middle panels show the two-dimensional spectrum where the *y*-axis is the slit (or spatial) direction and the *x*-axis is the dispersion direction. The bottom middle panels show the extracted one-dimensional spectrum after correcting for the rotation curve. The gray highlights are regions that are contaminated by skylines. The right-hand panels show the rotation curve of the galaxies, where the green line is the fitted rotation curve and the black markers are the measured centroids of the emission line at each spatial bin along the two-dimensional spectrum.

These reference spectra are then flux-calibrated so that their *V*-band magnitude is equal to the observed magnitude of the respective star. We mask the hydrogen lines in the flux-calibrated reference spectra and model their continuum using a similar step as above.

3. The correction factor at each wavelength is obtained by dividing the flux-calibrated spectrum by the observed telluric spectrum.

In general, we find that the correction factor for the ratio of [N II]$\lambda$6584 and H$\alpha$ ranges between 0.8 and 1.5. On average, the correction factor for the clumpy and nonclumpy sample is 1.05 and 1.09, respectively.

## 5. Comparison between Clumpy and Nonclumpy Galaxies

### 5.1. [N II]$\lambda$6584/H$\alpha$

Figure 4 shows four examples of the reduced one-dimensional, telluric-corrected spectrum. The flux for each emission line is obtained by fitting a double-Gaussian function using `lmfit`. To this end, we fix the relative wavelength offset between the two emission lines and assume that the line width for both lines are the same. Therefore, our fitting function consists of five parameters: the peak intensity ($a$) for both [N II] $\lambda$6584 and H$\alpha$, the line width ($\sigma$) for the emission lines, the wavelength center for H$\alpha$, and a constant continuum/background noise. The integrated flux for both emission lines is calculated as $a\sigma\sqrt{2\pi}$, using the respective line intensity. Similarly, the flux error is obtained by propagating the uncertainties of the fitted parameters $a$ and $\sigma$.

Out of the 42 galaxies, two galaxies are not detected in either H$\alpha$ and [N II]$\lambda$6584. Only 32 out of the remaining 40 galaxies have H$\alpha$ and [N II]$\lambda$6584 lines that are not significantly affected by atmospheric skylines, and have an SNR $> 3$. Table 1 lists their measured line ratios and their associated errors. We find the weighted average of the [N II]$\lambda$6584/H$\alpha$ ratio for the entire sample to be $0.36 \pm 0.01$. When separated into clumpy and nonclumpy sample, we find that clumpy

**Table 1**
Derived Values for the GNIRS Observations

| COSMOS ID | R.A. (deg) | Decl. (deg) | $z_{spec}$ | $\log(M_*)$ ($\log(M_\odot)$) | $\log(SFR_{UV+IR})$ ($\log(M_\odot\ yr^{-1})$) | $UV_{clumpy}$ | [N II]$\lambda$6584/H$\alpha$ | 12 + log(O/H) | $v_c$ (km s$^{-1}$) | $\sigma_0$ (km s$^{-1}$) |
|---|---|---|---|---|---|---|---|---|---|---|
| 2289 | 150.48253 | 1.7125193 | 0.712 | 10.44 | 0.99 | True | 0.26 ± 0.02 | 8.56 ± 0.02 | 172.3 ± 14.8 | 13.7 ± 6.1 |
| 40738 | 150.24486 | 1.9678429 | 0.936 | 10.44 | 1.45 | True | 0.21 ± 0.05 | 8.51 ± 0.06 | ⋯ | 35.8 ± 23.7 |
| 62945 | 149.72485 | 1.8760713 | 0.694 | 10.44 | 1.09 | True | 0.28 ± 0.07 | 8.58 ± 0.06 | ⋯ | ⋯ |
| 64167 | 149.66539 | 1.8908899 | 0.749 | 10.48 | 0.99 | False | 0.28 ± 0.06 | 8.58 ± 0.05 | ⋯ | ⋯ |
| 73816 | 150.5074 | 2.0096676 | 0.702 | 10.59 | 1.45 | False | 0.38 ± 0.04 | 8.66 ± 0.02 | 212.5 ± 22.2 | 4.1 ± 7.5 |
| 85093 | 150.67809 | 2.1846418 | 0.795 | 10.52 | 1.08 | True | 0.44 ± 0.14 | 8.70 ± 0.08 | ⋯ | ⋯ |
| 91389 | 150.72302 | 2.2811966 | 0.957 | 10.41 | 1.18 | True | 0.25 ± 0.07 | 8.55 ± 0.07 | ⋯ | 26.3 ± 17.1 |
| 91840 | 150.68439 | 2.2863963 | 0.607 | 10.61 | 1.08 | True | 0.49 ± 0.12 | 8.72 ± 0.06 | ⋯ | 21.5 ± 13.9 |
| 94152 | 150.4547 | 2.32392 | 0.662 | 10.58 | 0.93 | False | 0.37 ± 0.08 | 8.65 ± 0.06 | 186.7 ± 46.3 | 37.3 ± 20.4 |
| 111826 | 150.16794 | 2.099118 | 0.961 | 10.65 | 1.41 | False | 0.40 ± 0.08 | 8.67 ± 0.05 | ⋯ | 23.3 ± 15.2 |
| 116791 | 150.0715 | 2.1623764 | 0.662 | 10.57 | 1.53 | False | 0.42 ± 0.01 | 8.68 ± 0.01 | 108.2 ± 13.7 | 23.3 ± 7.0 |
| 118818 | 150.15173 | 2.1886752 | 0.927 | 10.56 | 1.70 | True | 0.27 ± 0.04 | 8.58 ± 0.04 | 151.5 ± 17.8 | 54.6 ± 7.5 |
| 118902 | 150.15822 | 2.1901271 | 0.925 | 10.51 | 1.57 | False | 0.34 ± 0.05 | 8.63 ± 0.04 | 179.7 ± 37.6 | 17.4 ± 12.4 |
| 120517 | 150.18661 | 2.2085881 | 0.892 | 10.47 | 1.52 | False | 0.41 ± 0.05 | 8.68 ± 0.03 | 201.8 ± 30.1 | 79.4 ± 13.1 |
| 121358 | 150.17503 | 2.2170861 | 0.679 | 10.42 | 1.31 | True | 0.27 ± 0.02 | 8.57 ± 0.01 | 173.3 ± 28.7 | 35.7 ± 6.9 |
| 122592 | 150.14954 | 2.2334945 | 0.731 | 10.35 | 1.16 | True | 0.27 ± 0.03 | 8.58 ± 0.03 | 68.2 ± 15.0 | 21.3 ± 7.7 |
| 122650 | 150.07106 | 2.2330399 | 0.603 | 10.53 | 1.28 | False | 0.39 ± 0.02 | 8.67 ± 0.01 | 167.4 ± 20.6 | 14.8 ± 6.7 |
| 123666 | 150.21819 | 2.2458375 | 0.657 | 10.61 | 1.36 | True | 0.42 ± 0.02 | 8.69 ± 0.01 | 255.1 ± 16.3 | 40.0 ± 10.6 |
| 125867 | 150.36453 | 2.2735415 | 0.749 | 10.41 | 1.24 | True | 0.22 ± 0.05 | 8.53 ± 0.05 | 127.1 ± 36.3 | 32.1 ± 12.4 |
| 127326 | 150.17822 | 2.292134 | 0.748 | 10.42 | 1.40 | True | 0.34 ± 0.09 | 8.63 ± 0.06 | ⋯ | 49.9 ± 20.1 |
| 151806 | 149.88297 | 2.1179976 | 0.677 | 10.49 | 0.94 | True | 0.30 ± 0.04 | 8.61 ± 0.03 | 149.4 ± 15.1 | 28.4 ± 8.6 |
| 153139 | 149.73523 | 2.1352146 | 0.698 | 10.43 | 1.18 | True | 0.41 ± 0.04 | 8.68 ± 0.02 | 171.7 ± 17.1 | 33.4 ± 11.0 |
| 159971 | 149.61758 | 2.215559 | 0.675 | 10.54 | 1.12 | False | 0.49 ± 0.06 | 8.72 ± 0.03 | 190.9 ± 19.4 | 16.2 ± 11.8 |
| 161993 | 149.8849 | 2.2384937 | 0.703 | 10.55 | 1.40 | False | 0.66 ± 0.05 | 8.80 ± 0.02 | ⋯ | ⋯ |
| 162807 | 149.75438 | 2.2461481 | 0.730 | 10.59 | 1.21 | True | 0.40 ± 0.14 | 8.67 ± 0.08 | ⋯ | ⋯ |
| 185948 | 150.51099 | 2.5288169 | 0.852 | 10.56 | 1.19 | False | 0.38 ± 0.15 | 8.66 ± 0.09 | ⋯ | ⋯ |
| 191595 | 150.53107 | 2.6109066 | 0.815 | 10.53 | 1.40 | False | 0.51 ± 0.09 | 8.73 ± 0.04 | ⋯ | ⋯ |
| 192043 | 150.65984 | 2.6178505 | 0.891 | 10.5 | 1.23 | True | 0.31 ± 0.07 | 8.61 ± 0.05 | ⋯ | 35.6 ± 23.1 |
| 207078 | 149.98328 | 2.4797268 | 0.704 | 10.5 | 1.40 | True | 0.30 ± 0.03 | 8.60 ± 0.02 | 75.9 ± 26.2 | 20.0 ± 9.2 |
| 207362 | 150.17223 | 2.4845951 | 0.800 | 10.48 | 1.24 | False | 0.53 ± 0.09 | 8.74 ± 0.04 | ⋯ | ⋯ |
| 239578 | 149.84 | 2.5136211 | 0.679 | 10.6 | 1.43 | False | 0.48 ± 0.05 | 8.72 ± 0.03 | 220.0 ± 26.6 | 15.6 ± 11.2 |
| 239638 | 149.72881 | 2.515331 | 0.696 | 10.43 | 1.03 | True | 0.30 ± 0.07 | 8.60 ± 0.06 | 145.6 ± 23.1 | 38.8 ± 14.7 |

**Note.** We list derived values only for galaxies where the H$\alpha$ and [N II]$\lambda$6584 emission lines are detected with an SNR greater than 3. The [N II]$\lambda$6584/H$\alpha$ line ratio is used to obtain the gas-phase metallicity using the calibration from M. Pettini & B. E. J. Pagel (2004). Missing values for both $v_c$ (rotational velocity, corrected for inclination) and $\sigma_0$ mean that no kinematic model was fitted to the 2D spectrum, while missing values for $v_c$ means that the inclination of the galaxy could not be constrained.

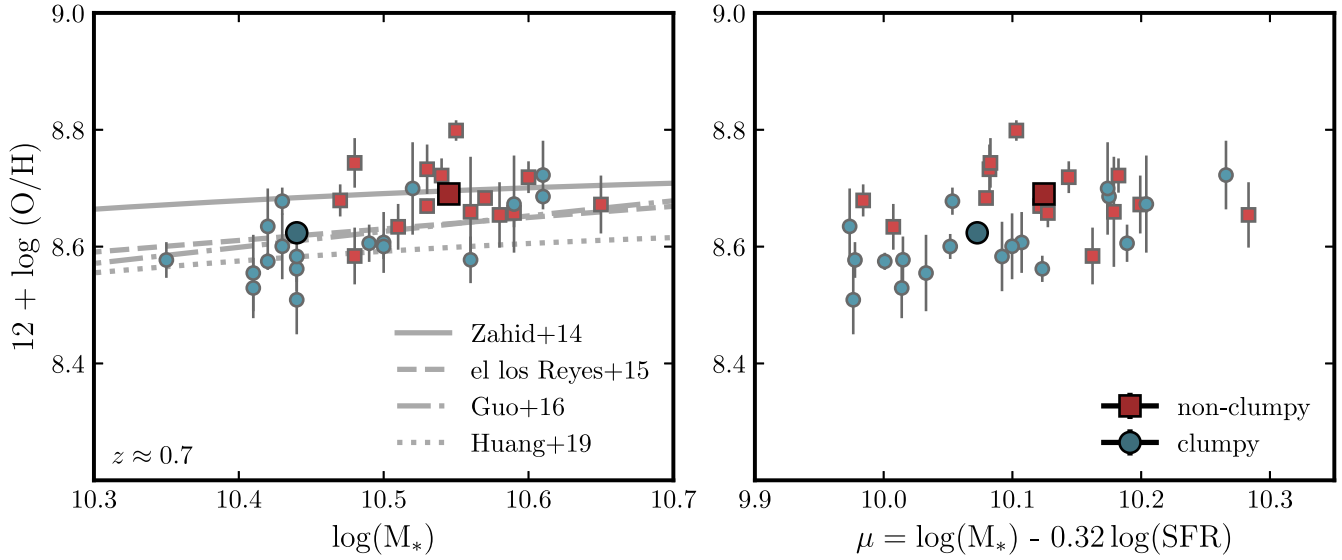


**Figure 5.** Left-hand panel: the metallicities of clumpy and nonclumpy galaxies in relation to stellar masses. The dark, larger markers show the weighted average. The different lines show the mass–metallicity relation for galaxies at $z \approx 0.8$ from H. J. Zahid et al. (2014), M. A. de los Reyes et al. (2015), Y. Guo et al. (2016), and C. Huang et al. (2019). The error is calculated as the weighted standard error. Right-hand panel: the metallicities in relation to the projected stellar masses and star formation rate.

galaxies have a weighted flux ratio average of 0.31 ± 0.02, while nonclumpy galaxies have a flux ratio of 0.42 ± 0.02. The difference in the [N II]λ6584 and Hα flux ratio is 0.11 ± 0.02. Taken at face value, this suggests a clear metallicity difference between the two samples; however, in the next section we examine this difference more closely via the mass–metallicity relation and the FMR.

### 5.2. The Mass–Metallicity Relation

The gas-phase metallicity of each galaxy is inferred by converting the [N II]λ6584/Hα line ratio to an oxygen abundance, using the N2 line ratio calibration from M. Pettini & B. E. J. Pagel (2004), which has the following form,

$$12 + \log(\mathrm{O/H}) = 8.9 + 0.57 \times \log([\mathrm{NII}]\lambda6584/\mathrm{H}\alpha). \quad (2)$$

This calibration is valid for $-2.5 < \log([\mathrm{NII}]/\mathrm{H}\alpha) < -0.3$. The error associated with the slope and intercept are 0.03 and 0.04, respectively. The [N II]λ6584/Hα line ratio and inferred metallicities are listed in Table 1.

The left side of Figure 5 shows the mass–metallicity relation for 32 SFGs with a detected SNR of at least three for both Hα or [N II]λ6584, color-coded as clumpy versus nonclumpy. The weighted averages are calculated using the inverse variance weighting, and are denoted as the dark, large markers, and their errors are calculated as the weighted standard error. We also plot the mass–metallicity relation from other studies for galaxies at a similar redshift range. However, since these studies used a different metallicity calibration, which can lead to discrepancies in metallicities (e.g., L. J. Kewley & S. L. Ellison 2008), we also apply a polynomial correction to each mass–metallicity relation to convert them to the N2 calibration. The polynomial correction are taken from H. Teimoorinia et al. (2021).

The gray curves are the corrected mass–metallicity relation from H. J. Zahid et al. (2014), M. A. de los Reyes et al. (2015), Y. Guo et al. (2016), and C. Huang et al. (2019), respectively. In general, we find that our values are consistent with other studies. Massive galaxies typically have higher metallicities, while lower-mass systems having lower metallicities. When split into a clumpy and nonclumpy sample, we find that the sample of clumpy SFGs have a lower median metallicity, with an offset of 0.07 ± 0.02 dex compared to their nonclumpy counterparts.

While the mass–metallicity relation of Figure 5 suggests a metallicity offset between clumpy galaxies and nonclumpy galaxies, we acknowledge that there is a small (but non-negligible) mass offset between the two samples. Our clumpy sample has a lower mean stellar mass compared to the nonclumpy galaxy sample. Although the original sample of targets were chosen so that both the stellar masses and star formation rates are similar, some galaxies were affected by skylines. This resulted in two samples of galaxies with a mean mass offset of 0.1 dex. However, we do not expect the mass difference to affect the observed metallicity offset by much since the mass–metallicity relations suggest only a slight change in metallicities with our given mass offset. For example, given the mass offset of 0.1 dex, the metallicity is expected to change by 0.01–0.02 based on the different mass–metallicity relations.

We further quantify this by fitting a mass–metallicity relation to our data. Using the analytical functions from H. J. Zahid et al. (2014), M. A. de los Reyes et al. (2015), Y. Guo et al. (2016), and C. Huang et al. (2019), we find the best fitting mass–metallicity relation for our observed metallicities by fixing the slope and only fitting the y-intercept. We opt to do this instead of fitting for both the slope and normalization factor due to our limited sample size and mass range. We find that the mass–metallicity relation from M. A. de los Reyes et al. (2015) gives the smallest scatter in the residuals. Figure 6 shows the histogram of the differences between the metallicity of clumpy and nonclumpy galaxies to the fitted mass–metallicity relation. A two-sample Kolmogorov–Smirnov (KS) test is performed on the two distributions to determine whether the distributions are statistically similar ($p > 0.05$) or different ($p \leqslant 0.05$). We obtain a $p$-value of 0.004, which rejects the null hypothesis of the same distribution.

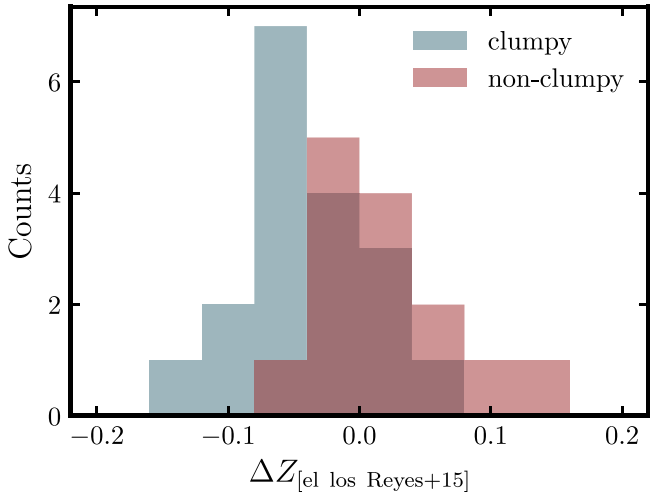


**Figure 6.** The histogram of the differences between the observed metallicity and the renormalized mass–metallicity relation from M. A. de los Reyes et al. (2015) for clumpy and nonclumpy galaxies. Using a KS test, we find the two distributions are statistically different, with a $p$-value of 0.004.

Finally, we note that the slope of the N2 relation from M. Pettini & B. E. J. Pagel (2004) is shallower (particularly at higher N2 regime—) relative to other N2 calibrations (e.g., R. A. Marino et al. 2013). This could lead to a more defined metallicity offset. To test whether the observed metallicity offset is affected by the choice of line calibration, we perform a similar KS test as above, but using metallicities derived from the steeper line calibration of R. A. Marino et al. (2013). Here, we obtain a $p$-value of 0.03. While the result is less significant than before, the null hypothesis that clumpy galaxies have the metallicities compared to nonclumpy galaxies can still be rejected.

### 5.3. The Fundamental Metallicity Relation

It is known that the gas-phase metallicity has a secondary dependence on the star formation rate of the galaxies. The metallicity is found to decrease with increasing SFR at a given stellar mass. The combined stellar mass, SFR, and metallicity is suggested to form a fundamental plane, and is known as the FMR (F. Mannucci et al. 2010). We use the following definition from F. Mannucci et al. (2010) to project the three-dimensional parameter space into two dimensions,

$$\mu = \log(M_*) - 0.32\log(\text{SFR}). \quad (3)$$

This projection of the FMR is chosen because it minimizes the scatter of the gas metallicity.

The right-hand side of Figure 5 shows the projected FMR for our galaxies. As shown in the figure, the distribution of $\mu$ for the clumpy and nonclumpy sample is slightly offset, with a mean difference of $\Delta\mu = 0.04$. When comparing the two distributions of $\mu$, a $p$-value of 0.21 is obtained, suggesting that the distributions of $\mu$ (i.e., the stellar masses and SFRs) for clumpy and nonclumpy galaxies are drawn from the same parent sample. However, if we perform a KS test on the metallicity distributions for clumpy and nonclumpy galaxies, we obtain a $p$-value of 0.004. These results suggest that lower metallicities in clumpy galaxies are not driven by the mass of the galaxies and/or their SFR, and are therefore intrinsic to the clumpy population.

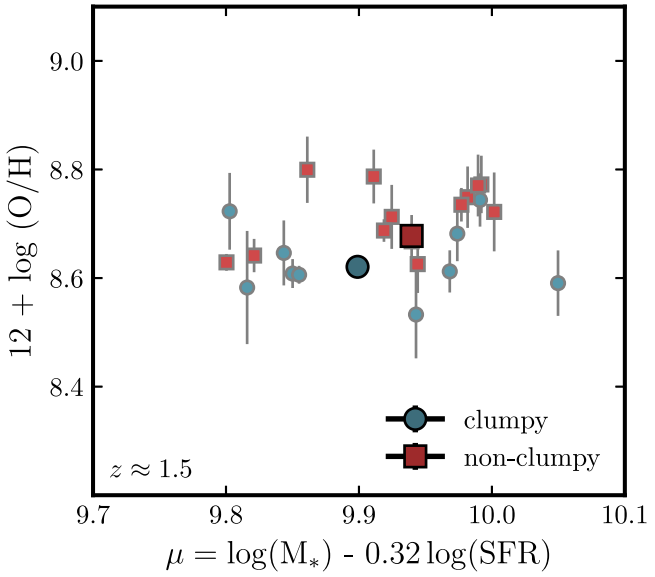


**Figure 7.** The FMR of clumpy and nonclumpy galaxies in the FMOS-COSMOS sample. The darker markers shows the weighted average and the error is taken as the weighted standard error. In general, the metallicity of clumpy and nonclumpy galaxies in the FMOS-COSMOS sample are similar to the GNIRS sample. The metallicity offset is measured to be 0.06 ± 0.02 dex.

### 5.4. Metallicity Difference in FMOS-COSMOS

In this section, we investigate whether there is a metallicity difference between clumpy and nonclumpy galaxies at a higher redshift. We use the [N II]$\lambda$6584 and H$\alpha$ observations from the FMOS-COSMOS survey, which targets galaxies at $z \approx 1.5$.

The selection criteria was described in Section 2.2. In essence, we select SFGs of similar masses, SFRs, and colors, with log(sSFR [yr$^{-1}$]) = −8.70 and −8.67 for clumpy and nonclumpy galaxies, respectively. Furthermore, only galaxies with a robust detection in H$\alpha$ and [N II]$\lambda$6584 are selected (SNR > 3). Since these galaxies are located in the COSMOS field, we use the deconvolved data set from V. Sok et al. (2022) to identify clumpy and nonclumpy galaxies (see Section 2.4). This results in a final sample size of 23 galaxies.

Figure 7 shows the relation between metallicities and the projected stellar masses and SFRs for clumpy and nonclumpy galaxies from the FMOS sample. In general, we find that the metallicities of the FMOS sample are comparable to our values. This is also in agreement with other studies of the FMR, which indicated that there is no observed evolution in the FMR with redshift (R. L. Sanders et al. 2021). We also find that clumpy galaxies have a lower median metallicity compared to nonclumpy galaxies, with an offset of 0.06 ± 0.02 dex. A similar two-sample KS test was performed on the metallicity distribution for clumpy and nonclumpy galaxies, and we obtain a $p$-value of 0.02. Given that the metallicity offset is observed at two different redshifts for a selected sample of galaxies with similar stellar masses and SFRs, these results suggest that clumpy galaxies intrinsically have lower metallicities compared to nonclumpy galaxies, and these differences cannot be explained by differences in their stellar mass or SFR alone.

## 6. Kinematics of Clumpy Galaxies

Having established that clumpy and nonclumpy galaxies have different metallicities, we now explore if additional signatures between the two samples are observed. Kinematics

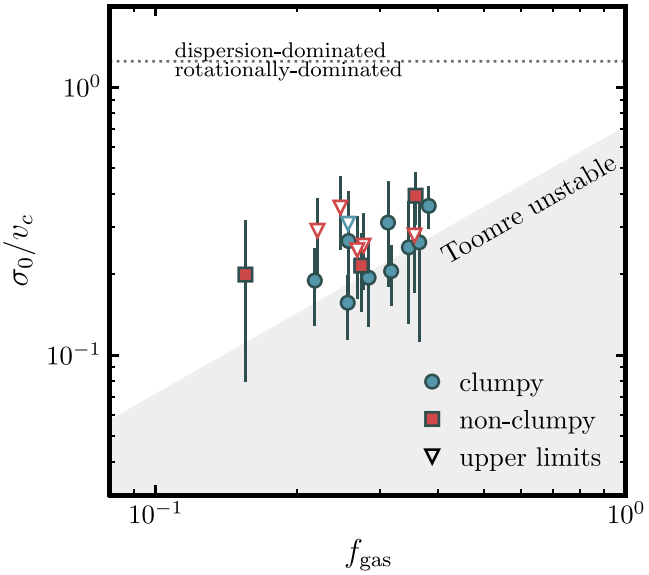


**Figure 8.** The relation between $\sigma_0/v_c$ and $f_{\rm gas}$ for clumpy and nonclumpy galaxies. $f_{\rm gas}$ is derived from the integrated SFR, using the Kennicutt–Schmidt relation. The darker color markers show the mean value and the error is calculated as the standard error of the mean. The dotted line shows the typical cutoff between rotationally and dispersion-dominated systems N. M. Förster Schreiber et al. (2009). The shaded region shows the parameter space in which the Toomre $Q$ value is less than 1 (i.e., unstable disks). This relation is defined by Equation (7) (see text for the derivation). Based on the integrated values, clumpy and nonclumpy galaxies have stable disks, with no significant differences between their kinematics.

are interesting because we might expect to see signs of increased disk instability in clumpy galaxies if clumps are formed via VDI. Figure 8 shows the relation between the gas fraction $f_{\rm gas}$ and $\sigma_0/v_c$. Here, $v_c$ is the asymptotic rotational velocity, corrected for the inclination of the galaxy (i.e., $v_c = v_a/\sin i$). The inclination $i$ is estimated as,

$$\cos i = \sqrt{\frac{q^2 - q_0^2}{1 - q_0^2}}. \tag{4}$$

Here, $q$ is the axial ratio of the galaxy, and $q_0$ is the intrinsic axial ratio for an edge-on galaxy, taken to be $q_0 = 0.2$ (B. S. Ryden 2006). The gas fraction is inferred using the relation between gas and SFR density (e.g., the Kennicutt–Schmidt relation; R. C. J. Kennicutt 1998). The SFR density is derived by assuming that star formation is contained within the effective radius. We obtain the effective radius and $q$ by fitting a Sérsic profile to the F814W images using `statmorph` (V. Rodriguez-Gomez et al. 2019). We further limit the analyses to "kinematically resolved" galaxies, where $v_c/\delta v_c$ is greater than 1 ($\delta v_c$ is the measurement uncertainty). We also note that some of the derived values $\sigma_0$ are unreliable due to our relatively coarse spectral resolution. In cases where the observed velocity dispersion is within one sigma uncertainty of the instrumental dispersion, we plot the observed dispersion (i.e., $\sigma_{\rm obs} = \sqrt{\sigma_0^2 + \sigma_{\rm inst}^2}$) as the upper limit for the intrinsic dispersion. These are denoted as open markers in the figure.

The dotted horizontal line in Figure 8 denotes the cutoff between dispersion-dominated and rotationally dominated disks, with the former having $\sigma_0/v_c > 1.25$ (e.g., N. M. Förster Schreiber et al. 2009). We find that both clumpy and nonclumpy galaxies have a range of kinematics, but can be viewed as rotationally dominated systems. Given the upper limits in the dispersion, it is also possible for the nonclumpy sample to have lower dispersion compared to clumpy galaxies.

The sloped line in Figure 8 is derived from the Toomre's $Q$ parameter (A. Toomre 1964). Instability within a gas disk is predicted when $Q$ falls before unity. $Q$ is typically expressed as,

$$Q = \frac{\sigma\kappa}{\pi G \Sigma_{\rm gas}}, \tag{5}$$

where $\sigma$ is the local dispersion, $\kappa$ is the epicyclic frequency, and $\Sigma_{\rm gas}$ is the gas density. $\kappa$ is related to the angular velocity $\Omega$ such that $\kappa = a\Omega$, and $a$ ranges from 1 for a Keplerian orbit to $\sqrt{3}$ for a uniform disk (A. Dekel et al. 2009b). As shown by R. Genzel et al. (2011), the Toomre parameter can then be reduced to,

$$\begin{aligned} Q &= \frac{\sigma\kappa}{\pi G\Sigma_{\rm gas}} = \frac{\sigma(av_c/R_{\rm disk})}{\pi G\Sigma_{\rm gas}} \\ &= a\left(\frac{\sigma}{v_c}\right)\left(\frac{v_c^2 R_{\rm disk}/G}{\pi R_{\rm disk}^2 \Sigma_{\rm gas}}\right) = a\left(\frac{\sigma}{v_c}\right)\left(\frac{M_{\rm tot}}{M_{\rm gas}}\right) \\ Q &= a f_{\rm gas}^{-1}\frac{\sigma}{v_c}, \end{aligned} \tag{6}$$

and $f_{\rm gas}$ is the gas fraction. Assuming a flat rotation with $a = \sqrt{2}$, the following equation is obtained

$$\frac{\sigma}{v_c} = Q\frac{f_{\rm gas}}{\sqrt{2}}. \tag{7}$$

Setting $Q = 1$ for the instabilitiy criterion gives the sloped relation in Figure 8. Lower values for $Q$ indicate unstable disks (i.e., the shaded region). Taking Figure 8 at face value, it appears that nonclumpy galaxies might be more kinematically stable than clumpy galaxies; however, given that many nonclumpy galaxies have only upper limits in the dispersion, we do not find a strong preference for clumpy galaxies to have lower Toomre values compared to nonclumpy galaxies.

It is not surprising that most galaxies are found to be marginally stable with $Q \sim 1$ if we consider the result within the context of a self-regulating disk. If the gas is accreted smoothly such that there is no injection of turbulence, $Q < 1$ is more readily achieved in the outer region of the disk given the increase in gas density and flatter rotation curve. This naturally leads to the fragmentation and formation of clumps. Several processes can then regulate $Q$ by driving up turbulence. Clump–clump interaction can lead to the transport of mass centrally, and the gain in gravitational energy during this process can increase gas turbulence. Similarly, clumpy accretion of gas is also suggested to drive up turbulence.

It is important to address several caveats in this analysis. We note that the use of $Q$ here only accounts for the gaseous component of the disk. An effective $Q$ that takes into account both the gaseous and stellar component may better predict the stability of the disk. For example, M. Puech (2010) found that while clumpy galaxies at $z \sim 0.6$ have $Q_{\rm gas}$ that is stable, their $Q_{\rm eff}$ is below unity. Likewise, Equation (5) describes the local instability within a gas disk. Since we are assuming a gas fraction that is derived from the integrated SFR, using the Kennicutt–Schmidt relation to estimate the gas fraction may be incorrect because clumpy galaxies have localized star formation. Similarly, the kinematics are measured based on the ionized gas, which can be susceptible to processes such as

outflows. It may be insightful to do similar analyses in the future at higher resolution with molecular gas observations because such observations can provide better constraints.

## 7. Discussion

### 7.1. Gas Inflow Driving the MZR Offset

The simplest explanation for the metallicity offset between galaxies of similar masses and SFRs is with the accretion of metal-poor gas; either induced by mergers, or cosmological gas accretion. Indeed, simulations have shown that the scatter in the mass–metallicity relation can be reproduced as the variations in SFR and metallicity (P. Torrey et al. 2018). The fluctuation of the gas supply can play a role in these variations, where lower gas inflow leads to the increase of metallicity (G. De Lucia et al. 2020). Similarly, van Loon et al. (2021) found that gas inflow influences the scatter of the mass–metallicity the most compared to other parameters such as outflows and star formation rate in the EAGLE simulation.

Observationally, lower metallicities in high-redshift ($z \approx 3$) galaxies can also be explained through gas accretion. By using a chemical evolution model from D. K. Erb (2008), G. Cresci et al. (2010) found that the relation between their observed metallicities and the inferred gas fraction is better explained as the accretion of in-falling pristine gas as opposed to outflows due to AGN or stellar winds. In this model, both the accretion and outflow rate is assumed to be a constant inflow and outflow fraction compared to the SFR. In the former case, this can be viewed as a continuous process or average of discrete accretion event. Similarly, using the MUSE data from the MEGAFLOW survey, I. Langan et al. (2023) found that galaxies with inflows are typically found at the lower end of the mass–metallicity relation.

### 7.2. Clump Formation Due to Gas Accretion

Chemical inhomogeneities in the gas disk have been observed both locally and at high-redshift, with localized, kiloparsec starbursts reportedly having lower metallicities compared to the surrounding regions (e.g., J. Sánchez Almeida et al. 2015). In the context of cosmological gas accretion, lower metallicities in such clumpy galaxies can be explained through the accretion of pristine gas. Such metal-poor gas accretion can either trigger a starburst as the gas compresses through its approach to the disk or result in a build up of the gas disk, which may subsequently form star-forming clumps due to internal instabilities. Using a zoom-in AMR cosmological simulation, D. Ceverino et al. (2016) found that the accretion of gas leads to the formation of star-forming clumps in galaxies with $M_* < 10^9 M_\odot$. In particular, in all the cases where clumps have a metallicity drop compared to the surrounding interstellar medium, the gas mass of the host galaxies steeply increases and can double prior to clump formation. Most of their observed clumps have a metallicity drop of around 0.3 dex and are typically dispersed within a few dynamical times.

### 7.3. Clump Formation Due to Mergers

Wet mergers have also been shown to lead to a dilution of metal contents in galaxies, with major mergers resulting in a larger metallicity drop in comparison to minor mergers (S. Bustamante et al. 2018). This study found that the metallicity dilution can range from approximately 0.05, 0.1, and 0.15 dex for minor (mass ratio $<1/10$), intermediate ($1/10 <$ mass ratio $< 1/3$), and major (mass ratio $> 1/3$) mergers, respectively. Our observed metallicity offset of 0.06–0.07 dex for both the GNIRS and FMOS sample suggests that both minor and immediate mergers could be the main driver for clump formation. This is broadly consistent with other studies that suggested that clump formation could be formed to minor mergers at low-redshift. In particular, the major merger rate is relatively low at $z \sim 1$, and is therefore not expected to be a major contributor of clump formation, while minor mergers are still relatively common at $z \sim 1$ (e.g., Y. Guo et al. 2015; T. Shibuya et al. 2016). It should also be noted that the galaxy major merger rate is expected to be higher toward high-$z$ (M. Romano et al. 2021; T. Shibuya et al. 2022; Q. Duan et al. 2024). Clumps observed at $z > 4$ (e.g., T. Shibuya et al. 2016; B. Ribeiro et al. 2017; K. N. Hainline et al. 2024) could therefore be formed due to major mergers. In fact, Y. Nakazato et al. (2024) found that most of their detected clumps at the redshift range of 5.5 and 9.5 were induced by mergers using the FirstLight simulation. We note that most of our galaxies are rotationally dominated, which may imply that the observed metallicity offset is not driven by major mergers. However, such kinematics signatures may not be a good indicator for major mergers because the galaxies may also be in their late merger stage.

### 7.4. What Are the Properties of the Host Star-forming Galaxies?

Within the picture of gas inflow, the accreting gas would lead to the dilution of metallicity and a burst of star formation. This relation between UV-bright, star-forming clumps and lower metallicities is also observed in our results. Figure 9 show the relation between the mean [N II]$\lambda$6584/H$\alpha$ line ratio as a function of the fractional rest-frame UV contribution from all clumps in a galaxy compared to the integrated value of its host galaxy for both the GNIRS and FMOS samples. The fractional UV contribution can be taken as the size and/or number of the clumps, where higher values can indicate that a galaxy hosts more and/or massive clumps. We find a slight correlation between the [N II]$\lambda$6584/H$\alpha$ line ratio and fractional rest-frame UV contribution. A Spearman correlation test yields a coefficient of $-0.47$ with a $p$-value of approximately 0.006. This result indicates that galaxies with a higher fractional UV contribution from clumps tend to have lower metallicities.

In addition, if gas accretion helps build up the disk of the galaxies, leading to VDI, we would expect the galaxies to have a disk-like morphology. The relation between clumpy and disk-like morphologies is reported by T. Shibuya et al. (2016), who observed that the clumpy fraction is higher for galaxies with lower Sérsic $n$ index (i.e., $n \sim 1$ indicates a disk-like component). A. Martin et al. (2023) reported no significant differences between the Sérsic index between clumpy and nonclumpy galaxies. We perform a similar analysis on our sample. Figure 10 shows the relation between the Sérsic index and the effective radius to the fractional UV contribution. Our analysis indicates that most of our galaxies exhibit disk-like structures. Additionally, we identify a slight correlation between the fractional $UV_{\rm rest}$ contribution of clumps and the Sérsic index of the galaxies. Utilizing the Spearman correlation coefficient test, we obtain a coefficient of $-0.44$, with a corresponding $p$-value of 0.01. On the other hand, the fractional

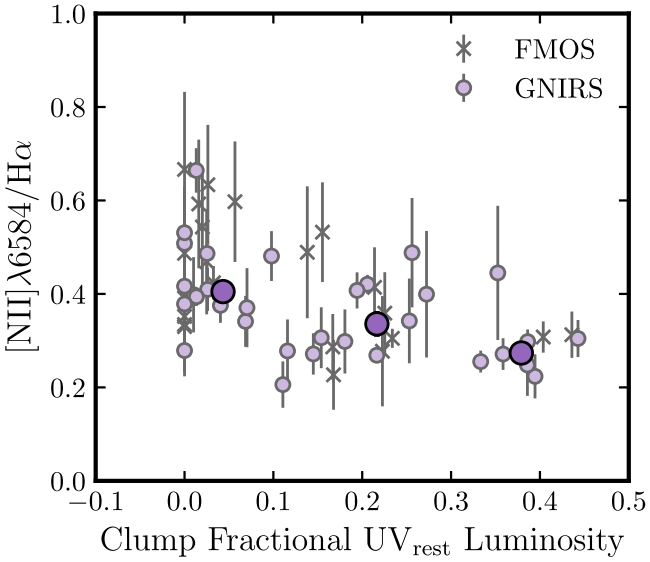


**Figure 9.** The relation between the [N II]$\lambda$6584/H$\alpha$ line ratio and the fractional UV$_{rest}$ contribution for the GNIRS and FMOS samples. The fractional UV$_{rest}$ contribution is defined as the ratio of the total rest-frame UV luminosity of all clumps in a galaxy to the total rest-frame UV luminosity of the galaxy. The darker markers show the mean fractional UV$_{rest}$ contribution and the weighted mean N2 line ratio for the GNIR sample, using discrete bins along the fractional UV$_{rest}$ contribution at between 0–0.15, 0.15–0.3, and 0.3–0.5. Each bin, starting from the lowest bin, has 14, 6, and 6 galaxies. If the fractional UV$_{rest}$ contribution is taken as the size/number of clumps in galaxies, the result suggests that clumpier galaxies are more likely to have lower metallicities.

UV$_{rest}$ contribution of clumps is correlated with the effective radius of the galaxies, with a Spearman coefficient of 0.78 ($p$-value $< 0.001$), suggesting that clumpier galaxies are larger in size. This can be explained within the framework of VDI (e.g., see A. Dekel et al. 2009b). First, gas accretion is anticipated to accumulate in the outer regions of the disk, leading to increased gas density in these areas. With smooth accretion, gas turbulence would remain unaffected. Finally, assuming a flat rotation curve, the angular velocity is expected to fall off as $\Omega \sim r^{-1}$. Together, these factors naturally lead to a decreasing Toomre parameter, $Q \sim \sigma\Omega/\Sigma$. We note that the relation between the size and fractional UV$_{rest}$ contribution could also be an observational artifact where it is easier to identify clumps that are further extended from the central regions of the galaxies.

## 8. Conclusion

Star-forming clumps in high-redshift SFGs are suggested to form as the result of violent disk instabilities within the gas-rich disk. Such disks are believed to be sustained by the continuous accretion of pristine gas from cosmological stream. If pristine gas accretion leads to clump formation due to VDI, we expect to find lower metallicities in clumpy galaxies.

In this work, we obtain the [N II]$\lambda$6584/H$\alpha$ line ratio for a sample of 32 SFGs at $z \approx 0.7$ and 23 SFGs at $z \approx 1.5$ in the COSMOS field in order to validate the above scenario by testing whether clumpy galaxies have lower metallicities compared to nonclumpy galaxies. The sample of galaxies consists of both clumpy and nonclumpy galaxies that are selected to have similar stellar masses and star formation rates. The classification of clumpy and nonclumpy is made based on whether or not the galaxy hosts clumps that account for more than 8% of the total rest-frame UV luminosity of the galaxy.

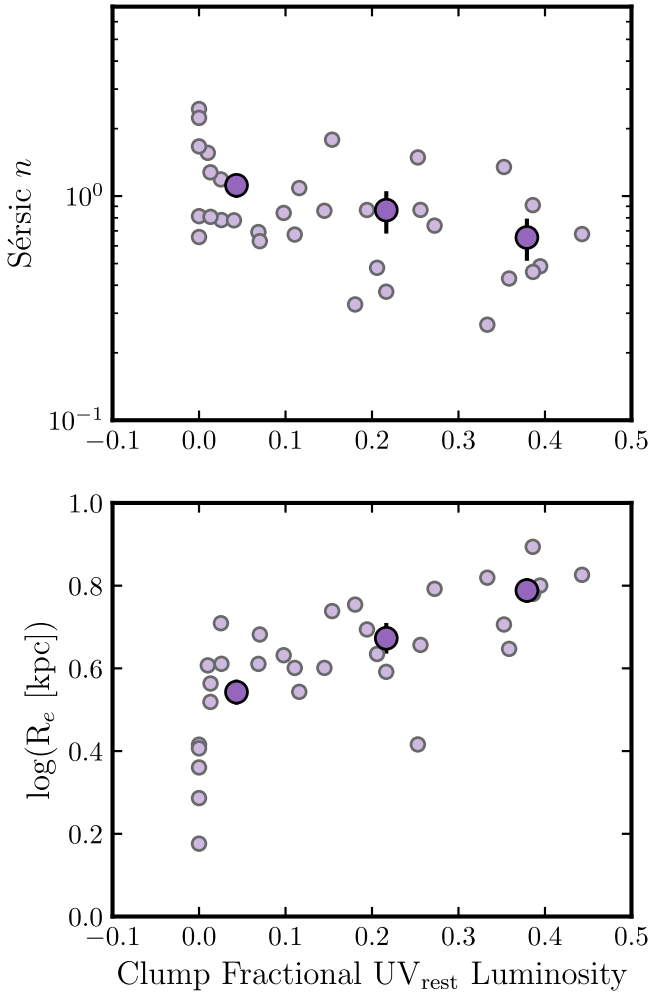


**Figure 10.** Similar to Figure 9, but now showing the comparison between the Sérsic index (top panel) and $R_e$ (bottom panel) to the fractional UV$_{rest}$ contribution of clumps. The darker markers now denote the mean, and the error here is taken as the standard error.

We infer the gas-phase metallicity based on the line ratio of [N II]$\lambda$6584 and H$\alpha$. The main takeaways of this paper are as follows.

1. We measure the mass–metallicity relation and find that it is in agreement with other studies of the relation at similar redshift ranges. Our weighted metallicity average is 8.67 $\pm$ 0.01 dex.
2. Clumpy galaxies have lower metallicities compared to nonclumpy galaxies, with a difference in the metallicity of 0.07 $\pm$ 0.02 dex.
3. Furthermore, we find a similar metallicity offset at a higher redshift by performing similar analyses using data from the FMOS-COSMOS survey. FMOS-COSMOS contains fluxes for both H$\alpha$ and [N II]$\lambda$6584 for galaxies in the COSMOS field at $z \approx 1.5$. We apply the same morphological classification to these galaxies and observe a metallicity offset of 0.06 $\pm$ 0.02 dex.
4. Both clumpy and nonclumpy galaxies exhibit a wide range of disk kinematics, with $\sigma_0/v_c$ ranging between 0.02 and 0.4. This indicates that the majority of our SFGs are rotationally dominated.

5. We do not find a significant difference in the kinematics of clumpy and nonclumpy galaxies.
6. The [N II]$\lambda$6584/H$\alpha$ ratio is negatively correlated with the fractional $UV_{rest}$ luminosity contribution from clumps. Interpreting the fractional $UV_{rest}$ luminosity as the number and/or size of clumps, this result suggests that "clumpier" galaxies tend to have lower metallicities.

Our results indicate a metallicity offset between clumpy and nonclumpy galaxies, as well as a clear relation between metallicity and the number of clumps. These results suggest that clump formation is driven by the inflow of metal-poor gas and that the processes that form them may not require significant kinematics instability in the gas disk. However, given the observational uncertainties, performing similar analyses with direct molecular gas observations would be valuable to provide better constraints for these parameters.

## Acknowledgments

The authors would like to thank the referee for the constructive feedback. G.W. gratefully acknowledges support from the National Science Foundation through grant AST-2205189 and from HST program number GO-16300. This paper is based on observations obtained at the international Gemini Observatory, a program of NSF's NOIRLab, which is managed by the Association of Universities for Research in Astronomy (AURA) under a cooperative agreement with the National Science Foundation on behalf of the Gemini Observatory partnership: the National Science Foundation (United States), National Research Council (Canada), Agencia Nacional de Investigación y Desarrollo (Chile), Ministerio de Ciencia, Tecnologìa e Innovación (Argentina), Ministério da Ciência, Tecnologia, Inovações e Comunicações (Brazil), and Korea Astronomy and Space Science Institute (Republic of Korea).

*Facility:* Gemini:Gillett (GNIRS).

*Software:* `astropy` (Astropy Collaboration et al. 2013, 2018; Astropy Collaboration et al. 2022), `emcee` (D. Foreman-Mackey et al. 2013), `lmfit` (M. Newville et al. 2016), `specutils` (N. Earl et al. 2022), `statmorph` (V. Rodriguez-Gomez et al. 2019).

## ORCID iDs

Visal Sok https://orcid.org/0000-0003-0780-9526
Adam Muzzin https://orcid.org/0000-0002-9330-9108
Pascale Jablonka https://orcid.org/0000-0002-9655-1063
Vivian Yun Yan Tan https://orcid.org/0000-0002-3503-8899
Z. Cemile Marsan https://orcid.org/0000-0002-7248-1566
Danilo Marchesini https://orcid.org/0000-0001-9002-3502
Gillian Wilson https://orcid.org/0000-0002-6572-7089
Leo Y. Alcorn https://orcid.org/0000-0002-2250-8687

## References

Adamo, A., Bradley, L. D., Vanzella, E., et al. 2024, Natur, 632, 513
Adams, D., Mehta, V., Dickinson, H., et al. 2022, ApJ, 931, 16
Agertz, O., Teyssier, R., & Moore, B. 2009, MNRAS, 397, L64
Astropy Collaboration, Price-Whelan, A. M., Lim, P. L., et al. 2022, ApJ, 935, 167
Astropy Collaboration, Price-Whelan, A. M., Sipőcz, B. M., et al. 2018, AJ, 156, 123
Astropy Collaboration, Robitaille, T. P., Tollerud, E. J., et al. 2013, A&A, 558, A33
Brammer, G. B., van Dokkum, P. G., & Coppi, P. 2008, ApJ, 686, 1503
Bustamante, S., Sparre, M., Springel, V., & Grand, R. J. J. 2018, MNRAS, 479, 3381
Cantale, N., Courbin, F., Tewes, M., Jablonka, P., & Meylan, G. 2016a, A&A, 589, A81
Cantale, N., Jablonka, P., Courbin, F., et al. 2016b, A&A, 589, A82
Cappellari, M., & Copin, Y. 2003, MNRAS, 342, 345
Carton, D., Brinchmann, J., Contini, T., et al. 2018, MNRAS, 478, 4293
Cava, A., Schaerer, D., Richard, J., et al. 2018, NatAs, 2, 76
Ceverino, D., Dekel, A., & Bournaud, F. 2010, MNRAS, 404, 2151
Ceverino, D., Sánchez Almeida, J., Muñoz Tuñón, C., et al. 2016, MNRAS, 457, 2605
Chabrier, G. 2003, PASP, 115, 763
Claeyssens, A., Adamo, A., Richard, J., et al. 2023, MNRAS, 520, 2180
Cresci, G., Mannucci, F., Maiolino, R., et al. 2010, Natur, 467, 811
de los Reyes, M. A., Ly, C., Lee, J. C., et al. 2015, AJ, 149, 79
De Lucia, G., Xie, L., Fontanot, F., & Hirschmann, M. 2020, MNRAS, 498, 3215
Dekel, A., Birnboim, Y., Engel, G., et al. 2009a, Natur, 457, 451
Dekel, A., Sari, R., & Ceverino, D. 2009b, ApJ, 703, 785
Dessauges-Zavadsky, M., & Adamo, A. 2018, MNRAS, 479, L118
Duan, Q., Conselice, C. J., Li, Q., et al. 2024, arXiv:2407.09472
Duncan, K., Conselice, C. J., Mundy, C., et al. 2019, ApJ, 876, 110
Earl, N., Tollerud, E., O'Steen, R., et al. 2022, astropy/specutils: v1.9.1, Zenodo, doi:10.5281/zenodo.7348235
Erb, D. K. 2008, ApJ, 674, 151
Foreman-Mackey, D., Hogg, D. W., Lang, D., & Goodman, J. 2013, PASP, 125, 306
Förster Schreiber, N. M., Genzel, R., Bouché, N., et al. 2009, ApJ, 706, 1364
Förster Schreiber, N. M., Renzini, A., Mancini, C., et al. 2018, ApJS, 238, 21
Gemini Observatory & AURA, 2016 Gemini IRAF: Data Reduction Software for the Gemini Telescopes, Astrophysics Source Code Library, ascl:1608.006
Genzel, R., Newman, S., Jones, T., et al. 2011, ApJ, 733, 101
Gillman, S., Tiley, A. L., Swinbank, A. M., et al. 2021, MNRAS, 500, 4229
Guo, Y., Ferguson, H. C., Bell, E. F., et al. 2015, ApJ, 800, 39
Guo, Y., Koo, D. C., Lu, Y., et al. 2016, ApJ, 822, 103
Guo, Y., Rafelski, M., Bell, E. F., et al. 2018, ApJ, 853, 108
Hainline, K. N., Johnson, B. D., Robertson, B., et al. 2024, ApJ, 964, 71
Horne, K. 1986, PASP, 98, 609
Huang, C., Zou, H., Kong, X., et al. 2019, ApJ, 886, 31
Huertas-Company, M., Guo, Y., Ginzburg, O., et al. 2020, MNRAS, 499, 814
Kashino, D., Silverman, J. D., Sanders, D., et al. 2019, ApJS, 241, 10
Kennicutt, R. C. J. 1998, ApJ, 498, 541
Kewley, L. J., & Ellison, S. L. 2008, ApJ, 681, 1183
Langan, I., Zabl, J., Bouché, N. F., et al. 2023, MNRAS, 521, 546
Mannucci, F., Cresci, G., Maiolino, R., Marconi, A., & Gnerucci, A. 2010, MNRAS, 408, 2115
Marino, R. A., Rosales-Ortega, F. F., Sánchez, S. F., et al. 2013, A&A, 559, A114
Martin, A., Guo, Y., Wang, X., et al. 2023, ApJ, 955, 106
Mowla, L., Iyer, K., Asada, Y., et al. 2024, arXiv:2402.08696
Murata, K. L., Kajisawa, M., Taniguchi, Y., et al. 2014, ApJ, 786, 15
Muzzin, A., Marchesini, D., Stefanon, M., et al. 2013, ApJS, 206, 8
Nakazato, Y., Ceverino, D., & Yoshida, N. 2024, ApJ, 975, 238
Newville, M., Stensitzki, T., Allen, D. B., et al., 2016 Lmfit: Non-linear Least-square Minimization and Curve-fitting for Python, Astrophysics Source Code Library, ascl:1606.014
Pettini, M., & Pagel, B. E. J. 2004, MNRAS, 348, L59
Pickles, A. J. 1998, PASP, 110, 863
Puech, M. 2010, MNRAS, 406, 535
Ribeiro, B., Le Fèvre, O., Cassata, P., et al. 2017, A&A, 608, A16
Rodriguez-Gomez, V., Snyder, G. F., Lotz, J. M., et al. 2019, MNRAS, 483, 4140
Romano, M., Cassata, P., Morselli, L., et al. 2021, A&A, 653, A111
Ryden, B. S. 2006, ApJ, 641, 773
Sánchez Almeida, J., Elmegreen, B. G., Muñoz-Tuñón, C., et al. 2015, ApJL, 810, L15
Sanders, R. L., Shapley, A. E., Jones, T., et al. 2021, ApJ, 914, 19
Sattari, Z., Mobasher, B., Chartab, N., et al. 2023, ApJ, 951, 147
Shibuya, T., Miura, N., Iwadate, K., et al. 2022, PASJ, 74, 73
Shibuya, T., Ouchi, M., Kubo, M., & Harikane, Y. 2016, ApJ, 821, 72
Silverman, J. D., Kashino, D., Sanders, D., et al. 2015, ApJS, 220, 12
Sok, V., Muzzin, A., Jablonka, P., et al. 2022, ApJ, 924, 7

Soto, E., de Mello, D. F., Rafelski, M., et al. 2017, ApJ, 837, 6
Tan, V. Y. Y., Muzzin, A., Marsan, Z. C., et al. 2022, ApJ, 933, 30
Teimoorinia, H., Jalilkhany, M., Scudder, J. M., Jensen, J., & Ellison, S. L. 2021, MNRAS, 503, 1082
Toomre, A. 1964, ApJ, 139, 1217
Torrey, P., Vogelsberger, M., Hernquist, L., et al. 2018, MNRAS, 477, L16
van Loon, M. L., Mitchell, P. D., & Schaye, J. 2021, MNRAS, 504, 4817
Vanzella, E., Castellano, M., Bergamini, P., et al. 2022, ApJL, 940, L53
Weiner, B. J., Willmer, C. N. A., Faber, S. M., et al. 2006, ApJ, 653, 1027
Wuyts, S., Förster Schreiber, N. M., Genzel, R., et al. 2012, ApJ, 753, 114
Wuyts, S., Förster Schreiber, N. M., Nelson, E. J., et al. 2013, ApJ, 779, 135
Zahid, H. J., Dima, G. I., Kudritzki, R.-P., et al. 2014, ApJ, 791, 130
Zanella, A., Le Floc'h, E., Harrison, C. M., et al. 2019, MNRAS, 489, 2792